Regime Diagrams of Solutions in an Idealized Quasi-Axisymmetric Model for Superrotation of Planetary Atmospheres

AUTHOR(S):

KASHIMURA, Hiroki; YODEN, Shigeo

CITATION:

KASHIMURA, Hiroki ...[et al]. Regime Diagrams of Solutions in an Idealized Quasi-Axisymmetric Model for Superrotation of Planetary Atmospheres. Journal of the Meteorological Society of Japan. Ser. II 2015, 93(2): 309-326

ISSUE DATE:

2015

URL:

http://hdl.handle.net/2433/218334

Journal of the Meteorological Society of Japan, Vol. 93, No. 2, pp. 309–326, 2015
DOI:10.2151/jmsj.2015-017

Regime Diagrams of Solutions in an Idealized Quasi-Axisymmetric Model for Superrotation of Planetary Atmospheres

Hiroki KASHIMURA

Institute of Space and Astronautical Science, Japan Aerospace Exploration Agency, Kanagawa, Japan

and

Shigeo YODEN

Graduate School of Science, Kyoto University, Kyoto, Japan

(Manuscript received 10 April 2014, in final form 7 January 2015)

Abstract

This paper presents regime diagrams illustrating the parametric dependence of dynamical balance in a superrotating atmosphere produced in a quasi-axisymmetric idealized system with strong horizontal diffusion studied previously by the present authors. In this system, the superrotation is maintained by the Gierasch mechanism, which possibly explains the four-day circulation in the atmosphere of Venus. Our previous paper developed a theoretical model of this system to estimate the superrotation strength and showed that the parametric dependence of the superrotation strength can be consolidated into three non-dimensional external parameters.

The present study analyzes the theoretical model to determine boundaries of the regimes based on the dynamical balance and plots theoretical regime diagrams, which are important to understand the non-linear dynamical system and are useful to clearly describe the parametric dependence. Further, a parametric limit of the theoretical model is also estimated and included in the diagrams. The parametric limit shows both a lower limit for the horizontal diffusion and an upper limit of the superrotation strength in the Gierasch mechanism. The regime diagram demonstrates that the superrotation in the cyclostrophic balance is realized when the horizontal Ekman number is in a certain range whose width is mainly controlled by the vertical Ekman number.

Numerical solutions covering a vast region in the parameter space are obtained by time-integrations of the primitive equations, and the dynamical regimes in the numerical solutions are compared with the theoretical regime diagrams. The theoretical regime diagrams agree well with the numerical results in most regions, confirming the validity of the theoretical model. Multiple equilibrium solutions are obtained when the horizontal Ekman number is lower than the theoretical limit. Moreover, they show that the Gierasch mechanism can maintain the superrotation even with the horizontal diffusion weaker than the predicted lower limit, but cannot generate superrotation from a motionless state.

Keywords regime diagram; superrotation; general circulation; planetary atmospheres

Corresponding author: Hiroki Kashimura (formerly known as Hiroki Yamamoto), Institute of Space and Astronautical Science, Japan Aerospace Exploration Agency, 3-1-1, Yoshinodai, Chuou, Sagamihara, Kanagawa 252-5210, Japan
E-mail: hiroki@gfd-dennou.org

1. Introduction

Superrotation, a state of an atmosphere that zonally rotates considerably faster than its solid planet, is a general circulation form of planetary atmospheres. Superrotation is observed in Venus and Titan, the

largest moon of Saturn. In both Venus and Titan, the zonal wind speed reaches approximately 100 m s^{-1} (e.g., Counselman III et al. 1980; Bird et al. 2005), which is 55 times faster than the planetary rotation speed at the equator in Venus and 8.3 times faster than that in Titan. The mechanism of the superrotation is still unclear even though many theoretical studies and numerical ones have been conducted (see e.g., Gierasch et al. 1997; Bengtsson et al. 2013 for reviews).

Gierasch (1975) presented an interesting mechanism for the superrotation by considering a quasi-axisymmetric system which describes the zonally averaged component of a 3D flow with a parameterization of non-axisymmetric eddy mixing by eddy diffusion (see Read 1986 for a review of the quasi-axisymmetric system applied to planetary atmospheres). Gierasch proposed that angular momentum is pumped vertically by mean meridional circulation and is transported toward the equator by the horizontal eddy diffusion; here, barotropic instability (Rossow and Williams 1979; Iga and Matsuda 1999; Luz and Hourdin 2003) or other horizontal shear instability with destabilized Kelvin modes (Iga and Matsuda 2005) may play the role of equatorward momentum transport which is represented by the eddy diffusion. At present, Gierasch's idea is one of the convincing hypotheses for the mechanism of the superrotation and is called "Gierasch mechanism."

Matsuda (1980, hereafter M80) explored the Gierasch mechanism by using a two-layer quasi-axisymmetric spectral model with only a few fundamental modes in meridional. He derived the parametric dependence of the superrotation strength which is defined as the ratio of the mean zonal wind to the planetary rotation speed at the equator. In addition, he showed a possibility of multiple equilibrium states in the general circulation of the Venus atmosphere for the first time. Another achievement of M80 is that he classified the system's solutions on the basis of their dynamical balance and drew regime diagrams showing the parametric dependence of the balance (Figs. 2, 4, 9, 10 in M80). The regime diagrams gave us a better understanding of the system. Although M80 obtained pioneering results, he as well as Gierasch (1975) assumed that the thermal advection by the mean meridional flow is negligible. Furthermore, M80 only showed regime diagrams for the condition that the timescale for the vertical diffusion is equal to that for radiative forcing (i.e., Newtonian heating and cooling). However, both the abovementioned assumption and condition may be unrealistic or too restrictive.

Our previous study, Yamamoto and Yoden (2013, hereafter YY13), relaxed the abovementioned assumption by allowing a decrease in the equator-to-pole temperature difference by the mean meridional thermal advection and theoretically estimated the superrotation strength maintained by the Gierasch mechanism. For this estimation, YY13 developed a quintic equation for a scalar measure of the superrotation strength from quasi-axisymmetric primitive equations. The quintic equation estimates the superrotation strength by its unique positive solution. In addition, the theoretical model expressed by the quintic equation shows that the superrotation strength depends only on the following three non-dimensional (combined) external parameters: the thermal Rossby number, the ratio of the timescale for radiative forcing to that for vertical diffusion, and the square of the ratio of the planetary rotation period to the geometric mean of the timescales for the horizontal and vertical diffusion. Such consolidation of the dependence on many physical parameters into that on a few non-dimensional parameters is useful for a simple treatment of the complex system, i.e., general circulations of planetary atmospheres.

YY13 obtained numerical solutions in steady- or statistically steady-states and showed that the theoretical estimation is valid for a wide parameter range. YY13 also investigated the dominant dynamical balance of the solutions and found that the balance can be classified into the following six types: a cyclostrophic, geostrophic, or horizontal diffusion balance with the equator-to-pole temperature difference nearly equal to that in a radiative-convective equilibrium state or with that significantly reduced by thermal advection.

For a better understanding of the nature of the general circulation of planetary atmospheres, we believe that comprehending the behavior of the non-linear dynamical system is very important. To comprehend the behavior of the system, exploring the parametric dependence of the solution and the dynamical balance is essential. A useful method to clarify the parametric dependence of the dynamical balance is to draw a regime diagram, which is a map of regimes in a parameter space, as M80 did. YY13 explored the superrotation strength and the dominant dynamical balance of the solution by constructing a theoretical model. However, the exploration was mainly focused on the parametric dependence on the external thermal Rossby number, which is inversely proportional to the square of the planetary rotation speed, and only four combinations were considered for the other two non-dimensional external parameters. One of the two parameters is proportional to the timescale for radiative forcing and the other is proportional to the

strength of horizontal diffusion. We believe that the dependence of the system on these parameters should be illustrated explicitly by regime diagrams and that the diagrams benefit readers for a better understanding of the system and for the application of the model.

In this study, we draw regime diagrams by defining the solution types based on the dominant balance. The diagrams are not restricted to the specific situation as in M80.

In YY13's theoretical model, as briefly reviewed in the following section, it was assumed that the time-scale for the horizontal diffusion is shorter than that for the meridional circulation. However, when the external thermal Rossby number is very high, the predicted meridional circulation becomes strong and may break this assumption. Such limitation was not considered in YY13, but it is important to clarify the applicable parametric range of the theoretical model. We investigate the limit on YY13's theoretical model in the parameter space and include it in the regime diagrams.

To verify the theoretically obtained regime diagrams and the limit, we perform time-integrations to obtain numerical solutions of the basic equations for a parameter region wider than that performed in YY13.

The possibility of multiple equilibrium states of the general circulation in planetary atmospheres was first pointed out by M80 and has become an important topic. Kido and Wakata (2008, 2009) succeeded in obtaining multiple equilibrium states in a 3D Venus-like general circulation model. Multiple equilibrium states in our 2D axisymmetric system were also obtained in YY13. However, only two examples were obtained in YY13. In this study, we obtain numerical solution for a wider parameter range, and multiple equilibrium states are obtained for more combinations of the external parameters than that in YY13. By investigating the distribution of multiple equilibrium states in the parameter space, we discuss the difference between the necessary condition for generating superrotation from a motionless state and that for simply maintaining it by the Gierasch mechanism. Such difference is important for explaining general circulation of real planetary atmospheres by the Gierasch mechanism as well as for performing simulation of the atmospheres of Venus and Titan.

In the following section, we provide a brief review of YY13 along with a description of the governing equations. The regime diagrams are theoretically obtained in Section 3. In Section 4, we perform numerical experiments to verify the theoretical regime diagrams using the numerical results of the primitive equations. Discussion including a comparison with M80 is presented in Section 5. Finally, a summary and conclusions are given in Section 6.

2. Brief review of Yamamoto and Yoden (2013)

2.1 Governing equations of the system

YY13 considered a quasi-axisymmetric 2D form of primitive equations for a dry Boussinesq fluid on a rotating hemisphere. The fluid is forced by Newtonian heating and cooling. The eddy diffusion terms of momentum and heat are formulated in analogy with molecular diffusion. However, following Gierasch (1975), YY13 assumed that the diffusion in horizontal direction efficiently transports momentum to homogenize angular velocity (i.e., down-gradient with respect to angular velocity) and that the horizontal heat transport by the diffusion is negligible. The governing equations are written as follows:

$$\frac{\partial u}{\partial t}+\frac{v}{a}\frac{\partial u}{\partial \phi}+w\frac{\partial u}{\partial z}-\frac{uv\tan\phi}{a}-2\Omega v\sin\phi = \nu_H D_H(u)+\nu_V\frac{\partial^2 u}{\partial z^2}, \tag{1}$$

$$\frac{\partial v}{\partial t}+\frac{v}{a}\frac{\partial v}{\partial \phi}+w\frac{\partial v}{\partial z}+\frac{u^2\tan\phi}{a}+2\Omega u\sin\phi = -\frac{1}{a}\frac{\partial \Phi}{\partial \phi}+\nu_H D_H(v)+\nu_V\frac{\partial^2 v}{\partial z^2}, \tag{2}$$

$$\frac{\partial \Phi}{\partial z}=g\frac{\theta-\Theta_0}{\Theta_0}, \tag{3}$$

$$\frac{\partial \theta}{\partial t}+\frac{v}{a}\frac{\partial \theta}{\partial \phi}+w\frac{\partial \theta}{\partial z}=-\frac{\theta-\theta_e}{\tau}+\kappa_V\frac{\partial^2 \theta}{\partial z^2}, \tag{4}$$

$$\frac{1}{a\cos\phi}\frac{\partial}{\partial \phi}(v\cos\phi)+\frac{\partial w}{\partial z}=0, \tag{5}$$

where

$$D_H(u)\equiv\frac{1}{a^2\cos\phi}\frac{\partial}{\partial \phi}\left(\cos\phi\frac{\partial u}{\partial \phi}\right)-\frac{u}{a^2\cos^2\phi}+\frac{2u}{a^2}, \tag{6}$$

$$D_H(v)\equiv\frac{1}{a^2\cos\phi}\frac{\partial}{\partial \phi}\left(\cos\phi\frac{\partial v}{\partial \phi}\right)-\frac{v}{a^2\cos^2\phi}+\frac{1}{a}\frac{\partial}{\partial \phi}\left[\frac{1}{a\cos\phi}\frac{\partial}{\partial \phi}(v\cos\phi)\right]+\frac{2v}{a^2}. \tag{7}$$

The variables u, v, and w are the zonal, meridional, and vertical components of the velocity, respectively; θ is the potential temperature; and $\Phi\equiv p'/\rho_0$, where p' is the dynamic pressure and ρ_0 is the constant density. The independent variables ϕ, z, and t are the latitude,

height, and time, respectively. The constant a is the planetary radius, Ω is the angular velocity of the planetary rotation, g is the gravitational acceleration, ν_H and ν_V are the horizontal and vertical diffusion coefficients of momentum, respectively, κ_V is the vertical thermal diffusion coefficient, τ is the time constant for Newtonian heating and cooling, and Θ_0 is a reference potential temperature. The values of ν_H, ν_V, κ_V, and τ are assumed to be constant for simplicity. The horizontal eddy diffusion terms, $D_H(u)$ and $D_H(v)$, are defined in a form so as to conserve angular momentum (Becker 2001) and are equivalent to those used in Gierasch (1975). The radiative-convective equilibrium potential temperature θ_e for Newtonian heating and cooling is given as $\theta_e \equiv \Theta_0[1-\Delta_H(\sin^2\phi - 1/3)]$, where Δ_H is the fractional change in potential temperature from the equator to the pole, and the global mean of θ_e is Θ_0.

The vertical boundary conditions are stress-free at the top boundary, no-slip at the bottom boundary, and no vertical mass or heat flux at both the top and the bottom boundaries. The lateral boundary conditions are no horizontal mass, momentum, or heat flux at both the equator and the pole, with the assumption of equatorial symmetry.

The form of the horizontal diffusion is a key assumption in this system. The horizontal diffusion term (6) in the zonal momentum equation acts in the direction of down-gradient with respect to angular velocity; that is, it can transport absolute angular momentum per unit mass defined by $M(\phi, z) \equiv [u(\phi, z) + a\Omega\cos\phi]a\cos\phi$ in its up-gradient direction. This feature is essential to generate and maintain the superrotation according to the Gierasch mechanism.

2.2 Theoretical model

YY13 developed a theoretical model consisting of the following four relationship equations:

$$R_{vB} \approx \pi^2 E_V S, \tag{8}$$

$$R_{vT} \approx \pi^2 E_V \left(\frac{S}{1+S}\right), \tag{9}$$

$$\frac{R_{vT} + R_{vB}}{2} \sim \frac{1}{\tau\Omega}\left(\frac{1}{\beta} - 1\right), \tag{10}$$

$$S^2 + 2S \sim 2\beta R_T - 20 E_H (R_{vT} + R_{vB}). \tag{11}$$

Here,

$$S \equiv \frac{U}{a\Omega}, \quad R_{vB} \equiv \frac{V_B}{a\Omega}, \quad R_{vT} \equiv \frac{V_T}{a\Omega}, \quad \text{and} \quad \beta \equiv \frac{\Delta\Theta}{\Theta_0 \Delta_H}, \tag{12}$$

are non-dimensional scalar variables that characterize the general circulation of planetary atmospheres; S represents the superrotation strength with U as a scale for the zonal wind at the top, R_{vB} and R_{vT} represent the Rossby numbers scaled with V_B and V_T as scales for the meridional winds just above the surface and at the top, respectively, and β represents the ratio of the equator-to-pole difference of vertically averaged potential temperature $\Delta\Theta$ to that in the radiative-convective equilibrium state $\Theta_0\Delta_H$. In the abovementioned equations,

$$E_V \equiv \frac{\nu_V}{H^2\Omega}, \quad E_H \equiv \frac{\nu_H}{a^2\Omega}, \quad \text{and} \quad R_T \equiv \frac{gH\Delta_H}{a^2\Omega^2}, \tag{13}$$

are the vertical Ekman number, horizontal Ekman number, and external thermal Rossby number, respectively. Here, H is the height of the top boundary. To derive the relationship equations from the governing equations (1)–(5), YY13 assumed a steady state ($\partial/\partial t = 0$) as well as the following scales and functions: $M_0(z) \equiv \int_0^{\pi/2} u(\phi, z) a\cos^2 d\phi = Ua[1-\cos(\pi z/H)]/2$ for the meridional integral of relative angular momentum, $u(\phi, H) = (3U/2)\cos\phi$ for the zonal wind at the top, $v(\phi, h) = -V_B \sin 2\phi$ and $v(\phi, H) = V_T \sin 2\phi$ for the meridional winds just above the surface and at the top, respectively, and $\bar{\theta}(\phi) \equiv \frac{1}{H}\int_0^H \theta(\phi, z) dz = \Theta_0 - \Delta\Theta(\sin^2\phi - 1/3)$ for the vertically averaged potential temperature.

YY13 obtained a quintic equation for the superrotation strength S by considering the relationship Eqs. (8)–(11) as a set of algebraic equations and by eliminating R_{vB}, R_{vT}, and β. The quintic equation is written as

$$\left[S^2 + 2S + BS\left(\frac{2+S}{1+S}\right)\right]\left[\frac{AS}{2}\left(\frac{2+S}{1+S}\right) + 1\right] = 2R_T, \tag{14}$$

where

$$A \equiv \pi^2 \tau\Omega E_V \quad \text{and} \quad B \equiv 20\pi^2 E_H E_V, \tag{15}$$

and R_T are positive constants that consist of external parameters. That is, the superrotation strength S explicitly depends only on R_T, A, and B. Here, R_T is the Rossby number scaled with the thermal wind at the top of the atmosphere with the equator-to-pole temperature difference of external radiative forcing; A is proportional to the ratio of the timescale for radiative forcing to that for vertical diffusion; and B is proportional to the square of the ratio of the planetary rotation period to the geometric mean of the time-

scales for the horizontal and vertical diffusion.

YY13 showed that the positive solution of Eq. (14) well-estimates the superrotation strength of numerical solutions of the governing equations for a wide parameter range.

2.3 *Dominant dynamical balance*

In addition, YY13 explored the dominant dynamical balance of the solution by simplifying the quintic Eq. (14) and rewriting it in a meridional momentum equation form as follows:

$$\underbrace{S^2}_{\mathrm{I}}+\underbrace{2S}_{\mathrm{II}}+\underbrace{BCS}_{\mathrm{III}}\approx\underbrace{2R_T\beta}_{\mathrm{IV}}, \tag{16}$$

where $C\equiv(2+S)/(1+S)$ was approximated to be a constant ($\because 1<C<2$) and β can be expressed as

$$\beta=\left(\frac{ACS}{2}+1\right)^{-1}, \tag{17}$$

by substituting Eqs. (8) and (9) into Eq. (10) and using A and C. The term I represents the metric term, II the Coriolis term, III the horizontal diffusion term acting on the meridional wind, and IV the pressure gradient term. From Eq. (16), YY13 indicated that the dominant balance must be between the term IV

$$\text{and}\begin{cases}\text{the term I when } S\gg 1,\ S\gg B\\ \qquad\cdots \text{ cyclostrophic balance [C]},\\ \text{the term II when } S\ll 1,\ B\ll 1\\ \qquad\cdots \text{ geostrophic balance [G]},\\ \text{the term III when } B\gg S,\ B\gg 1\\ \quad\cdots \text{ horizontal diffusion balance [H]}.\end{cases} \tag{18}$$

Furthermore, YY13 found that β can be approximated for the following two cases:

$$\beta\approx\begin{cases}1 & \text{when } AS\ll 1\cdots[1],\\ (0.5ACS)^{-1} & \text{when } AS\gg 1\cdots[0].\end{cases} \tag{19}$$

The former case [1] means that the equator-to-pole difference of the potential temperature $\Delta\Theta$ is almost equal to that of the basis potential temperature for Newtonian heating and cooling $\Theta_0\Delta_H$. In contrast, the latter case [0] means that $\Delta\Theta$ is significantly smaller than $\Theta_0\Delta_H$. Consequently, the typical dynamical balance in Eq. (16) was classified into six types of the combinations of [C, G, H] and [1, 0]. For example, C1 indicates the cyclostrophic balance with $\beta\approx 1$.

3. Regime diagrams of solutions in the system

Although YY13 explored the theoretical estimation of the superrotation strength S and the dominant dynamical balance, as reviewed in the previous section, the exploration was mainly focused on the parametric dependence on the external thermal Rossby number R_T, and only four combinations of A and B were considered (Fig. 7 in YY13). Remember that A is proportional to the ratio of the timescale for radiative forcing to that for vertical diffusion, and B is proportional to the square of the ratio of the planetary rotation period to the geometric mean of the timescales for the horizontal and vertical diffusion. To completely understand the behavior of this non-linear system, it is important to clarify the dependence on A and B in regime diagrams. We believe that such regime diagrams will be useful for a better understanding of the Gierasch mechanism and for investigating the superrotation of planetary atmospheres such as Venus and Titan. These regime diagrams would also be of interest to readers with a viewpoint of geophysical fluid dynamics.

3.1 *Definition of solution types*

To draw regime diagrams, we define solution types based on the dynamical balance that was considered in YY13 and summarized in Section 2.3. The previous study focused on the case when two dominant terms were nearly balanced in Eq. (16) and β is very close to or much less than unity; the classification was expressed by "$\ll$" or "$\gg$" as shown in Eqs. (18) and (19). Although Eq. (1) can be a three- or four-term balance, in this study, we classify the solutions into six types denoted by "XY," where X = C, G, or H, and Y = 1 or 0 are determined by the following conditions:

$$\max(S^2, 2S, BS)=\begin{cases}S^2 & (\text{i.e., } S>2, S>B) \Rightarrow X=\mathrm{C},\\ 2S & (\text{i.e., } S\le 2, B\le 2) \Rightarrow X=\mathrm{G},\\ BS & (\text{i.e., } B\ge S, B>2) \Rightarrow X=\mathrm{H},\end{cases} \tag{20}$$

and

$$\begin{cases}\beta>0.5 \Rightarrow Y=1,\\ \beta\le 0.5 \Rightarrow Y=0,\end{cases} \tag{21}$$

respectively. The same symbols as YY13 are used but the definitions are revised. Types CY, GY, and HY are redefined by the maximum term on the lhs of Eq. (16) with the assumption of C = 1 for simplicity. Note that the maximum term on the lhs always plays a major role in balancing the rhs (term IV) because all the terms are positive; CY, GY, and HY mean that the solution is in cyclostrophic, geostrophic, and horizontal diffusion balance, respectively. In the definitions of $X1$ and $X0$, β = 0.5 is used for the threshold.

Here, $X1$ (i.e., $\beta > 0.5$) means the thermal advection has a little impact on the equator-to-pole difference of the potential temperature; whereas, $X0$ (i.e., $\beta \leq 0.5$) means that has a significant impact on it.

3.2 Parametric limit on YY13's theoretical model

One of the assumptions in constructing the theoretical model in YY13 is that the relaxation time for horizontal diffusion is considerably shorter than the turnover time of the meridional circulation; YY13 introduced this assumption by following Gierasch (1975) and M80. The abovementioned condition can be written as $E_H \gg R_{vB}$. Here, the Rossby number scaled with the meridional wind just above the surface R_{vB} is used for the reciprocal of the non-dimensional turnover time because $R_{vB} > R_{vT}$ from Eqs. (8) and (9).

We should note that the theoretical model states:

1. The superrotation strength S increases according to the external thermal Rossby number R_T as shown in YY13's Fig. 2 and Eqs. (36) and (37).
2. R_{vB} is proportional to S, as given by Eq. (8).

If we use S instead of R_{vB} with Eq. (8), the abovementioned condition ($R_{vB} \ll E_H$) can be written as

$$S \ll \frac{E_H}{\pi^2 E_V}. \tag{22}$$

Therefore, under a high R_T condition, S exceeds $E_H/(\pi^2 E_V)$ and the abovementioned assumption breaks down, i.e., the theoretical model does not function. In other words, the upper limit of the superrotation strength could be given by

$$S = S_L \equiv \frac{E_H}{\pi^2 E_V} = \frac{B}{20\pi^4 E_V^2}. \tag{23}$$

3.3 Regime diagrams

In this subsection, we draw regime diagrams that show the solution types and the limit considered above in both R_T-A space and R_T-B space. Remember that $R_T = gH\Delta_H/(a^2\Omega^2)$, $A = \pi^2\tau\Omega E_V$, and $B = 20\pi^2 E_H E_V$ are external non-dimensional parameters controlling the superrotation strength in the model. First, we rewrite Eq. (14) with respect to R_T as

$$R_T(S, A, B) = \frac{1}{2}\left[S^2 + 2S + BS\left(\frac{2+S}{1+S}\right)\right]\left[\frac{AS}{2}\left(\frac{2+S}{1+S}\right)+1\right]. \tag{24}$$

Now, R_T can be considered to be a function of S, A, and B. In the following subsections, we derive equations describing the boundaries of the solution types and the parametric limit on the theoretical model.

a. Boundary between CY and GY

From definition (20), the boundary between the cyclostrophic balance CY and the geostrophic balance GY is $S = 2$ for $B \leq 2$, which means that the zonal wind speed at the top (U) is twice as fast as the rotation speed of the solid planet ($a\Omega$) and the metric term is equal to the Coriolis term in Eq. (16) with a smaller horizontal diffusion term. Substituting $S = 2$ into Eq. (24), we obtain the following equation for the boundary between CY and GY:

$$R_T(2, A, B) = \frac{4}{9}(B+3)(4A+3) \quad \text{for} \quad B \leq 2. \tag{25}$$

We would like to note that the boundary approaches a straight line in a logarithmic graph of R_T-A or R_T-B in the following cases:[1]

$$R_T \approx \begin{cases} 4 & \text{when} \quad A \ll 1 \quad \text{and} \quad B \ll 1, \\ 16A/3 & \text{when} \quad A \gg 1 \quad \text{and} \quad B \ll 1. \end{cases} \tag{26}$$

b. Boundary between CY and HY

The boundary between the cyclostrophic balance CY and the horizontal diffusion balance HY is $S = B$ for $B > 2$; therefore, we obtain

$$R_T(B, A, B) = \frac{B}{2}\left[B + 2 + B\left(\frac{2+B}{1+B}\right)\right]\left[\frac{AB}{2}\left(\frac{2+B}{1+B}\right)+1\right] \quad \text{for} \quad B > 2, \tag{27}$$

for the boundary equation, which can be approximated in the following cases:

$$R_T \approx \begin{cases} B^2 & \text{when} \quad AB \ll 1 \quad \text{and} \quad B \gg 1, \\ AB^3/2 & \text{when} \quad AB \gg 1 \quad \text{and} \quad B \gg 1. \end{cases} \tag{28}$$

c. Boundary between GY and HY

The boundary between the geostrophic balance GY and the horizontal diffusion balance HY is $B = 2$ but only when $S \leq 2$ such that the boundary equation is

$$B = 2 \quad \text{for} \quad R_T < R_T(2, A, 2) = \frac{20}{9}(4A+3). \tag{29}$$

[1]Note that some of the approximated forms of the boundaries shown here and below are slightly different from the forms of R_{T1} and R_{T2} shown in Table 1 of YY13. This is because YY13 considered the lhs of Eq. (16) separately (did not consider the sum of the three term in the lhs) during the approximation process; whereas, in this study, we use Eq. (24), which is derived from the quintic equation of the theoretical model without any approximations.

d. Boundary between X1 and X0

To obtain the equation for the boundary between the state that the thermal advection is negligible $X1$ and that is dominant $X0$, we substitute $\beta = 0.5$ into Eq. (17) and obtain the following equation:

$$AS^2 + 2(A-1)S - 2 = 0, \tag{30}$$

where C is replaced by $(2+S)/(1+S)$ in Eq. (17). Remember that β represents the ratio of the equator-to-pole difference of vertically averaged potential temperature $\Delta\Theta$ to that in the radiative-convective equilibrium state $\Theta_0\Delta_H$. Therefore, β = 0.5 means that the effect of radiative forcing and that of thermal advection to the equator-to-pole temperature difference is comparable. The positive solution of Eq. (30) is

$$S = S_{10} \equiv \frac{1}{A} - 1 + \sqrt{\frac{1}{A^2} + 1}. \tag{31}$$

Substituting S_{10} into Eq. (24), we obtain the equation for the boundary between $X1$ and $X0$ as follows:

$$\begin{aligned} &R_T(S_{10}, A, B) = \\ &\frac{1}{2}\left[S_{10}^2 + 2S_{10} + BS_{10}\left(\frac{2+S_{10}}{1+S_{10}}\right)\right]\left[\frac{AS_{10}}{2}\left(\frac{2+S_{10}}{1+S_{10}}\right)+1\right] \\ &= \frac{2}{A^2}\left(AB + 1 + \sqrt{1+A^2}\right). \end{aligned} \tag{32}$$

This equation's dependence on A changes from $R_T \propto A^{-2}$ to $R_T \propto A^{-1}$ as A increases. We can approximate the equation as follows:

$$R_T \approx \begin{cases} 4A^{-2} & \text{when} \quad A \ll 1 \quad \text{and} \quad AB \ll 1, \\ 2A^{-1}B & \text{when} \quad AB \gg 1 \quad \text{and} \quad AB \gg A, \\ 2A^{-1} & \text{when} \quad A \gg 1 \quad \text{and} \quad AB \ll A. \end{cases} \tag{33}$$

e. Boundary for the parametric limit

The boundary for the model's parametric limit, considered in Section 3.2, should be included into the regime diagrams. We use the upper limit of the superrotation strength S_L given by Eq. (23) as the boundary for breaking the inequality (22). Simply using S_L, we introduce the equation for the boundary as

$$\begin{aligned} &R_T(S_L, A, B) \\ &= \frac{1}{2}\left[S_L^2 + 2S_L + BS_L\left(\frac{2+S_L}{1+S_L}\right)\right]\left[\frac{AS_L}{2}\left(\frac{2+S_L}{1+S_L}\right)+1\right] \\ &= \frac{B}{40\pi^4 E_V^2}\left[\frac{B}{20\pi^4 E_V^2} + 2 + B\left(\frac{40\pi^4 E_V^2 + B}{20\pi^4 E_V^2 + B}\right)\right] \\ &\quad \times\left[\frac{AB}{40\pi^4 E_V^2}\left(\frac{40\pi^4 E_V^2 + B}{20\pi^4 E_V^2 + B}\right)+1\right]. \end{aligned} \tag{34}$$

Under the conditions of $S_L \gg 1$ and $S_L \gg B$, which are equivalent to $B \gg 20\pi^4 E_V^2$ and $1 \gg 20\pi^4 E_V^2$, the abovementioned equation can be approximated as

$$R_T \approx \begin{cases} S_L^2/2 = B^2/[2(20\pi^4 E_V^2)^2] \\ \quad \text{when} \quad AS_L \ll 1 \quad \text{or} \quad AB \ll 20\pi^4 E_V^2, \\ AS_L^3/4 = AB^3/[4(20\pi^4 E_V^2)^3] \\ \quad \text{when} \quad AS_L \gg 1 \quad \text{or} \quad AB \gg 20\pi^4 E_V^2. \end{cases} \tag{35}$$

The abovementioned equation shows not only the approximated form of the parametric limit of the theoretical model but also the lower limit of the strength of the horizontal diffusion, which is expressed by E_H, for the Gierasch mechanism. By substituting $S_L = E_H/(\pi^2 E_V)$ into Eq. (35) with some manipulations, we obtain

$$\begin{aligned} E_H &\approx E_{HL} \\ &\equiv \begin{cases} \sqrt{2}\pi^2 R_T^{\frac{1}{2}} E_V & \text{when} \quad A^2 \ll (2R_T)^{-1}, \\ \left(4\pi^4 R_T \dfrac{E_V^2}{\tau\Omega}\right)^{\frac{1}{3}} & \text{when} \quad A^2 \gg (4R_T)^{-1}. \end{cases} \end{aligned} \tag{36}$$

These equations estimate the lower limit of the horizontal Ekman number E_{HL} for given R_T, E_V, and $\tau\Omega$. This limit is important because the horizontal diffusion in the quasi-axisymmetric system is the parameterization of effects of non-axisymmetric eddies which are expected to transport angular momentum equatorward to maintain the superrotation.

f. Four regime diagrams as typical examples

Using Eqs. (25), (27), (29), (32), and (34), we can draw any regime diagram in non-dimensional parameter space (R_T, A, B, E_V). As typical examples, we show four cross sections of the parameter space on upper panels in Figs. 1 and 2. Here, the vertical Ekman number is fixed at $E_V = 10^{-3}$ because it does not explicitly affect Eqs. (25), (27), (29), and (32). By

fixing E_V, we can consider $A(=\pi^2\tau\Omega E_V)$ as a measure of the radiative timescale and $B(=20\pi^2E_HE_V)$ as a measure of strength of horizontal diffusion. The boundary equations described above are expressed by the following curves with line types: dotted for Eq. (25), dashed for Eq. (27), double-dot-dashed for Eq. (29), single-dot-dashed for Eq. (32), and solid for Eq. (34). The approximated forms of the boundary equations, i.e., Eqs. (26), (28), (33), and (35), are also shown along with the corresponding part of the curves. The region where the theoretical model will not work is indicated by NG, meaning "Non-Gierasch."

Figures 1a and 1b show R_T-A cross sections at $B = 2\pi^2 \times 10^{-2}$ and $B = 2\pi^2 \times 10^{0}$, respectively, which can be roughly considered as cross sections of the planetary rotation speed and the radiative timescale with horizontal Ekman number fixed at $E_H = 10^0$ and 10^2, respectively. In Fig. 1a, the horizontal diffusion balance HY does not appear because the horizontal diffusion is sufficiently weak to satisfy $B \leq 2$. In Fig. 1b, on the other hand, the geostrophic balance GY does not appear because $B > 2$, and the boundary for the parametric limit on the model also does not appear in this parameter range because of a high value of $E_H = 10^2$. In the lower A side below the single-dot-dashed curve, the dotted curve and the solid curve in Fig. 1a and the dashed curve in Fig. 1b approach $R_T = 4$, $S_L^2/2$, and B^2, respectively, which have no dependence on A. This shows that the dynamical balance and the upper limit of the superrotation strength do not depend on the radiative timescale if the radiative forcing is strong enough to maintain the temperature almost radiative-convective equilibrium.

We should note that, by definition, we obtained each boundary by substituting a certain value into the superrotation strength S in Eq. (24). Therefore, the boundaries in Figs. 1a and 1b, except the single-dot-dashed curve, also indicate constant S curves: $S = 2$ for dotted curve, $S = B$ for dashed curve, and $S = S_L = B/(20\pi^4E_V^2)$ for solid curve. Figures 1c and 1d display contours of S calculated from Eq. (14) for the same cross sections as the upper panels (a and b), respectively; NG region is indicated by shade. These figures show that for a given value of the external thermal Rossby number R_T, the superrotation strength decreases as the radiative timescale ($\tau \propto A$) increases, after A exceeds a certain value shown by the single-dot-dashed curve. Remember that the single-dot-dashed curve denotes the parametric location where the thermal advection decreases the equator-to-pole temperature difference by half (i.e., $\beta = 0.5$), as described in Subsection 3.3.c. Namely, as A increases, the superrotation strength starts decreasing after the timescale of thermal advection becomes comparable with the radiative timescale because of the decrease in the equator-to-pole temperature difference by thermal advection.

Figures 2a and 2b show R_T-B cross sections at $A = \pi^2 \times 10^{-2}$ and $A = \pi^2 \times 10^{0}$, respectively. Because we fixed E_V now, $B = 20\pi^2E_HE_V$ simply expresses the strength of the horizontal diffusion compared with the effect of planetary rotation. In both the cross sections, the region where the theoretical model will not function (NG) expands as B ($\propto E_H$) becomes lower. It is interesting that the cyclostrophic balance denoted by CY, which is the most likely balance for the atmosphere of Venus, is sandwiched between the horizontal diffusion balance HY and NG regions. That is, for the circulation to be the cyclostrophic balance, B has to be

$$20\pi^4E_V^2\left(\frac{4R_T}{A}\right)^{\frac{1}{3}} \leq B \leq \left(\frac{2R_T}{A}\right)^{\frac{1}{3}}, \tag{37}$$

or, in other words, E_H has to be

$$\pi^2E_V\left(\frac{4R_T}{A}\right)^{\frac{1}{3}} \leq E_H \leq \frac{1}{20\pi^2E_V}\left(\frac{2R_T}{A}\right)^{\frac{1}{3}}. \tag{38}$$

The abovementioned inequalities tell us that E_V mainly controls the width of the E_H range for the cyclostrophic balance; that is, the superrotation with the cyclostrophic balance is realized widely if the vertical diffusion is small. Note that the lhs of inequalities (38) is identical to the lower limit of the horizontal Ekman number E_{HL} for $A^2 \gg (4R_T)^{-1}$ case, as shown in Eq. (36). Figures 2c and 2d display contours of the superrotation strength S. In the GY and the CY regimes, the superrotation strength is not dependent on B (or horizontal diffusion E_H) and increases as R_T increases; whereas, in the HY regime, a higher R_T is necessary to maintain the same strength of superrotation.

4. Numerical experiments

4.1 Numerical procedure

Numerical solutions of the governing equations (1)–(5) are obtained by time-integrations of a discretized set of equations from an initial state of rest. Numerical methods are the same as those described in YY13 and are not repeated here. Numerical solutions are obtained for $R_T = 10^n$, where $n = -2, -1, 0, ..., 7$, with 14 combinations of the values of $A = \pi^2\tau\Omega E_V$ and $B = 20\pi^2E_HE_V$ with E_V fixed at 10^{-3}, as listed in

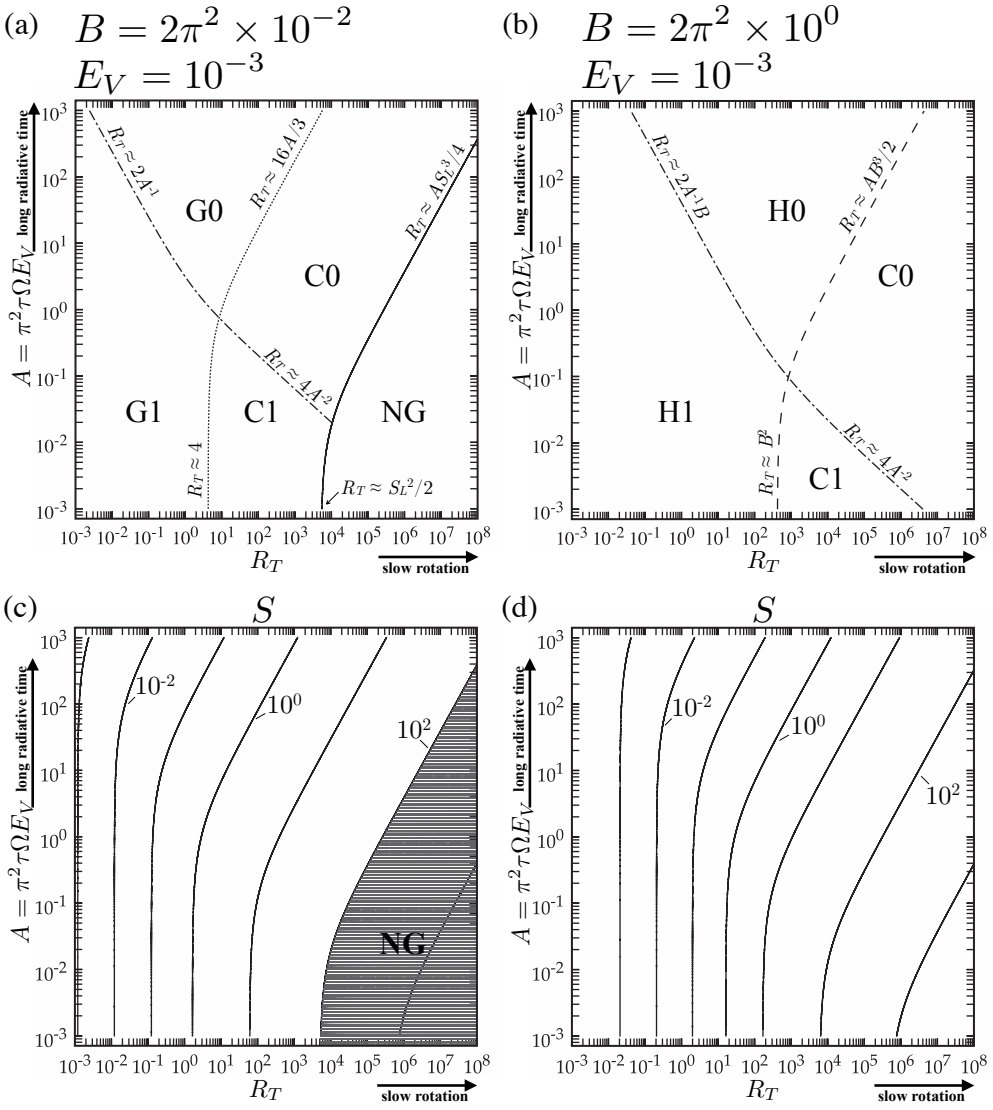

Fig. 1. Theoretical regime diagrams for R_T-A cross sections at (a) $B = 2\pi^2 \times 10^{-2}$, $E_V = 10^{-3}$ and (b) $B = 2\pi^2 \times 10^{0}$, $E_V = 10^{-3}$ (upper panels). The solution types are shown by C1, C0, G1, G0, H1, and H0. The region where the theoretical model (i.e., Gierasch mechanism) will not function is shown by NG. The boundaries are shown by curves: dotted for Eq. (25), dashed for Eq. (27), dot-dashed for Eq. (32), and solid for Eq. (34). Approximated form of the equations for the boundaries are also shown. Lower panels (c and d) show contours of S for $S = 10^{-3}$, 10^{-2}, 10^{-1}, ..., 10^{3} at the same cross sections as the upper panels. Shaded region indicates the NG region. Note that $A = \pi^2\tau\Omega E_V$ and $B = 20\pi^2 E_H E_V$.

Table 1. These combinations almost cover the regime diagrams (Figs. 1, 2) at an interval of one order of magnitude.

YY13 obtained multiple equilibrium states of two different solutions with two combinations of the non-dimensional parameters: (A, B, E_V, R_T) = ($\pi^2 \times 10^{-2}$, $2\pi^2 \times 10^{-2}$, 10^{-3}, 10^{5}) and ($\pi^2 \times 10^{-3}$, $2\pi^2$, 10^{-3}, 10^{4}). One equilibrium state has a weak shallow equatorial jet with strong meridional circulation as shown in Figs. 3 and 4 of YY13; the other has a strong deep equatorial jet with a nearly solid-body rotation state and weak meridional circulation, as shown in Fig. 6 of YY13. The latter state follows the present theoretical model but the former does not (i.e., the Gierasch

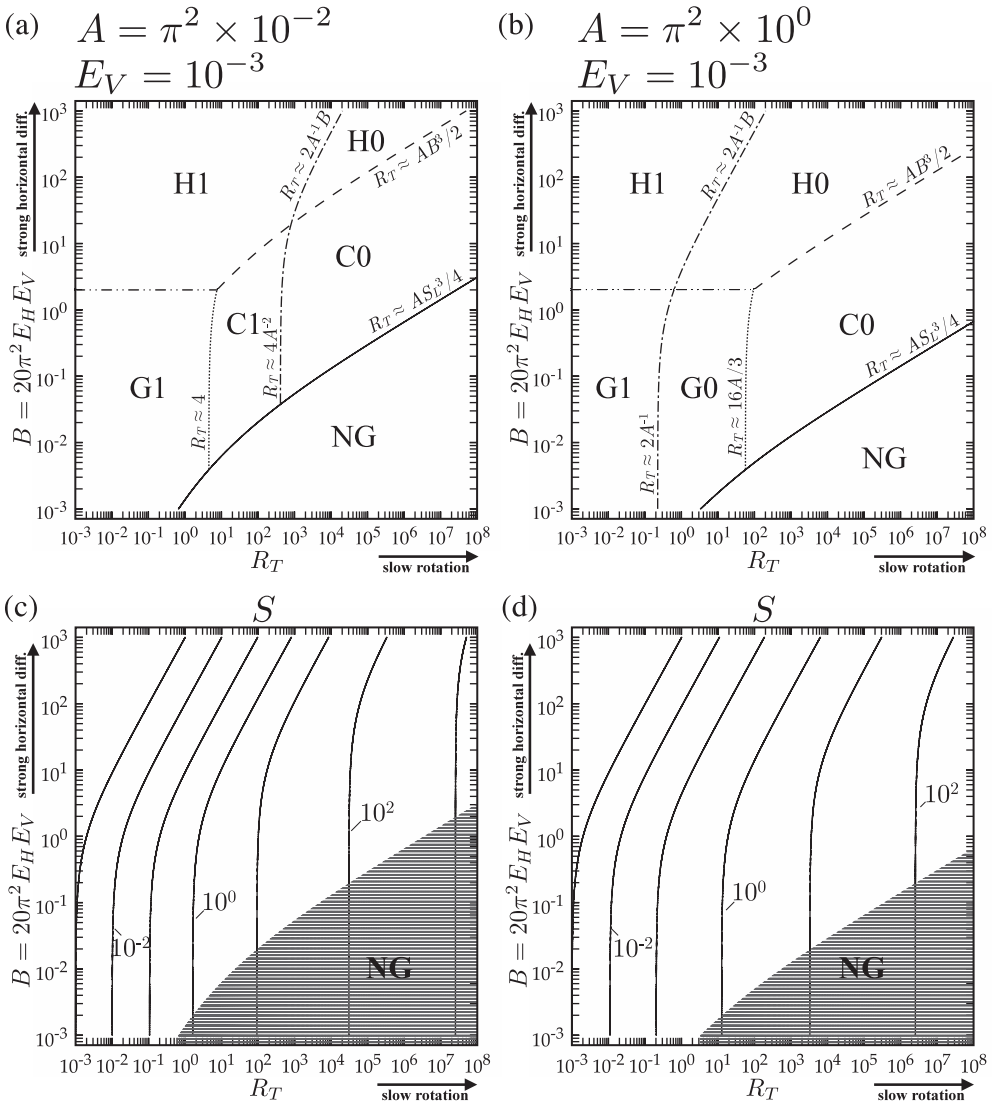

Fig. 2. Same as Fig. 1 but for R_T-B cross sections at (a) $A = \pi^2 \times 10^{-2}$, $E_V = 10^{-3}$ and (b) $A = \pi^2 \times 10^{0}$, $E_V = 10^{-3}$. Double-dot-dashed lines represent Eq. (29).

mechanism does not work). YY13 obtained the former state with time-integrations from an initial state of rest. The latter state was obtained by time-integrations from the statistically steady-state solution, which was superrotating, for R_T an order of magnitude lower. Following the results described above, we expect multiple equilibrium states may exist with the parameter values listed in Table 1 and attempt to obtain another equilibrium state with the same experimental procedure as YY13 if the numerical solution obtained from a state of rest has a weak shallow equatorial jet.

Following YY13, we calculate S_n and β_n (subscript n for numerical solutions) defined as

$$S_n \equiv \frac{1}{a\Omega}\sum_{j=1}^{J} u(\phi_j, z_K)\cos\phi_j \Delta\phi_j, \tag{39}$$

$$\beta_n \equiv \frac{1}{\Theta_0 \Delta_H}\sum_{k=1}^{K} \frac{\theta(\phi_1, z_k) - \theta(\phi_J, z_k)}{K}, \tag{40}$$

for each numerical solution. Here, $\phi_1, \phi_2, \phi_3, ..., \phi_J$ ($J = 64$) are the Gaussian latitudes from the equator to the pole, z_k ($k = 1, 2, 3, ..., K$; $K = 50$) is the altitude at each layer from the bottom to the top,

Table 1. Values of A, B and E_V for the numerical experiments. Here, $A = \pi^2\tau\Omega E_V$ and $B = 20\pi^2 E_H E_V$, and the used values of $\tau\Omega$ and E_H are also listed. Asterisks indicate repetitions in the list.

	A	B	E_V	$\tau\Omega$	E_H
1)	$\pi^2\times10^{1}$	$2\pi^2\times10^{-2}$	10^{-3}	10^{4}	1
2)	$\pi^2\times10^{0}$			10^{3}	
3)	$\pi^2\times10^{-1}$			10^{2}	
4)	$\pi^2\times10^{-2}$			10	
5)	$\pi^2\times10^{-3}$			1	
6)	$\pi^2\times10^{1}$	$2\pi^2\times10^{0}$		10^{4}	10^{2}
7)	$\pi^2\times10^{0}$			10^{3}	
8)	$\pi^2\times10^{-1}$			10^{2}	
9)	$\pi^2\times10^{-2}$			10	
10)	$\pi^2\times10^{-3}$			1	
*9)	$\pi^2\times10^{-2}$	$2\pi^2\times10^{0}$		10	10^{2}
11)		$2\pi^2\times10^{-1}$			10
*4)		$2\pi^2\times10^{-2}$			1
12)		$2\pi^2\times10^{-3}$			10^{-1}
*7)	$\pi^2\times10^{0}$	$2\pi^2\times10^{0}$		10^{3}	10^{2}
13)		$2\pi^2\times10^{-1}$			10
*2)		$2\pi^2\times10^{-2}$			1
14)		$2\pi^2\times10^{-3}$			10^{-1}

$\Delta\phi_j \equiv (\phi_{j+1}-\phi_{j-1})/2$, where $j = 2, 3, 4, ..., J-1$, $\Delta\phi_1 \equiv (\phi_2+\phi_1)/2$, and $\Delta\phi_J \equiv (\pi-\phi_J-\phi_{J-1})/2$. By substituting S_n and β_n into Eqs. (20) and (21), respectively, we determine the solution type for each numerical solution.

4.2 *Solution types of numerical results*

Figures 3 and 4 show the distribution of the types of numerical solutions by symbols on the same cross sections in the parameter space as in Figs. 1 and 2, respectively. A lack of symbols denotes that the numerical solutions were not obtained because of numerical instability, and finer resolution may be needed. The theoretical borders of the solution types are also shown by curves (same as the upper panels of Figs. 1, 2).

The theoretical regime diagrams agree with the distribution of the numerically obtained solution types in most regions, as shown in Figs. 3 and 4. This is because S_n and β_n are well-estimated by the theoretical model (not shown, see Figs. 7, 9 of YY13).

Disagreement between the numerical results and the theoretical regime diagrams appears in high R_T regions. In Fig. 3a, multiple equilibrium states are obtained in the NG region, where the predicted meridional turnover time is shorter than the timescale for the horizontal diffusion. Time-integrations from the initial state of rest achieved steady solutions in which the Gierasch mechanism does not work as the theoretical model stated; however, the superrotation in a nearly solid-body rotation is maintained by the Gierasch mechanism when the initial condition is a superrotation state. Each state has a similar feature as that showed in M80 with the highly-truncated model, i.e., the former state has a weak jet with strong meridional circulation and the latter has a strong jet with weak meridional circulation. The multiple equilibrium states are obtained in the same manner as YY13 as well as Kido and Wakata (2008, 2009), who obtained multiple equilibrium states in a 3D Venus-like general circulation model. In Fig. 3b, disagreement occurs in a high R_T and low A region; NG solutions (cross signs) appear though $E_H = 10^2$ is very high and the theoretically predicted S satisfies Eq. (22). In other words, the Gierasch mechanism did not work even with a very strong horizontal diffusion ($E_H = 10^2$) in an atmosphere with slow planetary rotation ($R_T \geq 10^6$) and short radiative time ($A \leq 10^0$). Note that the fourth row ($A = \pi^2\times10^{-2}$) of symbols in Fig. 3b corresponds to the first row in Fig. 4a, which shows an R_T-B cross section of the parameter space. The two panels show that the theoretical model tends to disagree with the numerical results when A is low and both B and R_T are high. Figure 4b shows another disagreement in the parameter region of relatively weak horizontal diffusion ($B = 2\pi^2\times10^{-3}$) and slow rotation ($R_T \geq 10^5$). In this region, the numerical solution follows the theoretical model (C0 type), even though it is outside the boundary for the parametric limit we considered in Section 3.3.e (NG region).

5. Discussion

5.1 *Comparison with Matsuda (1980)*

The regimes of the solution of the quasi-axisymmetric model in which the Gierasch mechanism works were originally explored by M80. He considered the following three cases: the case with horizontal diffusion of infinite magnitude acting only on the zonal wind (his Section 3), same as the first case but with finite magnitude (his Section 4), and the case with finite horizontal diffusion acting equally on both the zonal and meridional winds (his Section 5)[2]. Because our system exhibits horizontal diffusion both in zonal and meridional momentum equations with the same

[2]In Section 5 of M80, the same horizontal diffusion acted also on the temperature field. However, its effects in his model were not described in details and seemed to be canceled in his regime diagram given by Fig. 10 of M80.

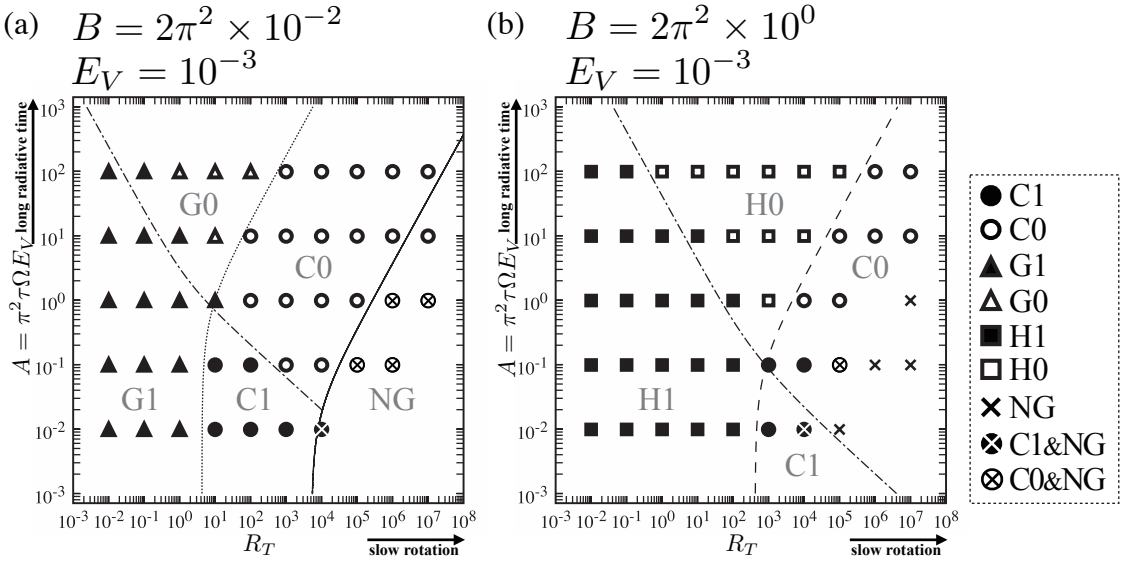

Fig. 3. Distribution of the types of the numerical solutions on R_T-A cross sections at (a) $B = 2\pi^2 \times 10^{-2}$, $E_V = 10^{-3}$ and (b) $B = 2\pi^2 \times 10^{0}$, $E_V = 10^{-3}$. The solution types are shown by symbols (see the legend). A cross sign indicates the solution in which the Gierasch mechanism did not work. Curves show the theoretically obtained boundaries of the regimes (same as the upper panels of Fig. 1).

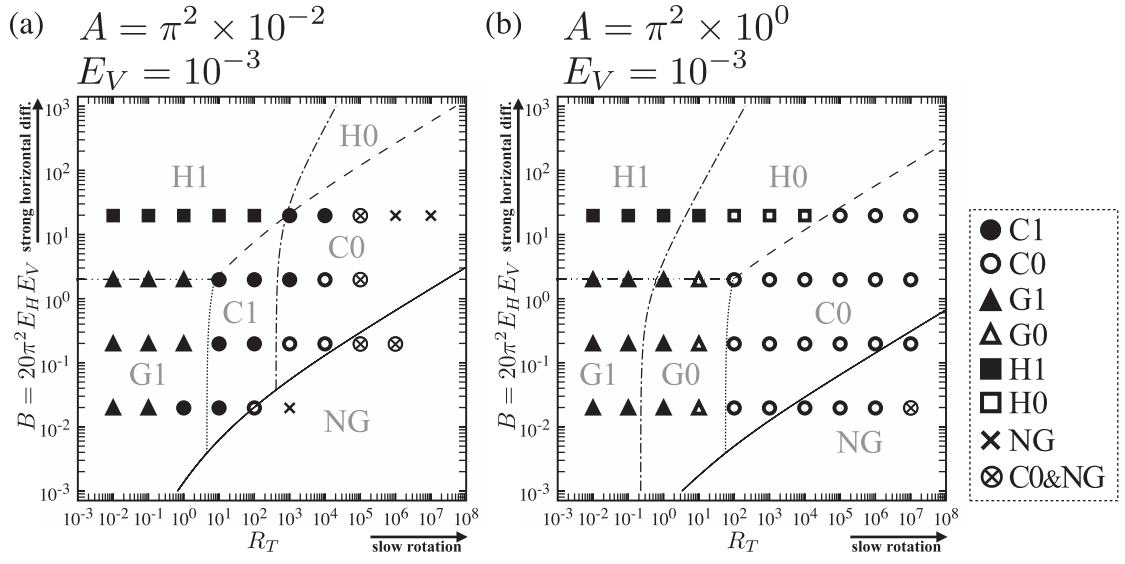

Fig. 4. Same as Fig. 3 but for R_T-B cross sections at (a) $A = \pi^2 \times 10^{-2}$, $E_V = 10^{-3}$ and (b) $A = \pi^2 \times 10^{0}$, $E_V = 10^{-3}$.

finite magnitude, we could refer to M80's third case for a comparison of regime diagram.[3] Even for the third case, there are some differences with the present study in the theoretical model, the classification of the solutions, and both the cross section and parameter space

[3]Note that, in YY13, the estimated superrotation strength was compared with the second case of M80. This was because his main result estimating the upper limit of the superrotation strength was shown in his second case.

used for illustrating the regime diagram. We discuss them below.

The theoretical model in M80 did not include the effect of thermal advection by the mean meridional flow, whereas we have included it. We have assumed statically neutral states for the basis potential temperature θ_e; therefore, the effect of thermal advection by the mean vertical flow has been negligible. On the other hand, M80 assumed a strong stratification and included the effect of vertical thermal advection in his model. However, most of the description in M80 was devoted to the condition that the temperature field was basically determined by the radiative processes and the effect of thermal advection were negligible.

For the classification of the solutions, M80 introduced three types based on the dynamical balance: thermal wind balance of the Venus type (V), thermal wind balance of the Earth type (E), and direct cell balance (D). Here, the types V, E, and D could, respectively, correspond to the cyclostrophic (C1), the geostrophic (G1), and the horizontal diffusion (H1) balance with the equator-to-pole temperature difference almost equal to that of external forcing (i.e., effects of thermal advection are negligible) in this study. Note that the type D could be the balance between the pressure gradient term and the horizontal diffusion term in the meridional momentum equation for M80's third case, although the horizontal diffusion was replaced by the vertical one in the definition of type D for the other two cases in M80 (see his Section 5). Because M80 did not include the effect of the meridional thermal advection, the counterparts of C0, G0, and H0 (equator-to-pole temperature difference is significantly reduced by the meridional thermal advection in types *X*0) do not exist in M80.

To draw a regime diagram, M80 considered the situation that the timescale for the vertical diffusion is equal to that for radiative timescale; that is,

$$E_V^{-1} = \tau\Omega, \tag{41}$$

in a non-dimensional form. In addition, M80 assumed the ratio of the timescale for the horizontal diffusion to that for the vertical one to be constant and much less than unity; that is,

$$E_V / E_H = \text{const.} \ll 1, \tag{42}$$

in a non-dimensional form. Under the above constraint and assumption, M80 drew the regime diagram by using $2\pi E_V$, which is now equivalent to $2\pi/(\tau\Omega)$, for the horizontal axis and $\sqrt{G_r}$ for the vertical axis, where G_r is the Grashof number multiplied by the square of the aspect ratio [see Eq. (3.14) in M80 for the definition]. M80 considered the horizontal axis $2\pi E_V$ as a measure of planetary rotation and the vertical axis $\sqrt{G_r}$ as a measure of the meridional temperature difference of radiative thermal forcing. On the other hand, we have shown the regime diagrams by fixing $E_V = 10^{-3}$ in R_T-A cross section and R_T-B one (Figs. 1–4). Remember that $R_T = gH\Delta_H/(a^2\Omega^2)$ is the external thermal Rossby number, $A = \pi^2\tau\Omega E_V$ is the non-dimensional measure of timescale for radiative forcing, and $B = 20\pi^2 E_H E_V$ is that for horizontal diffusion with fixed E_V.

For comparison with the regime diagram in M80, we attempt to draw a theoretical regime diagram with M80's constraint and assumption in the following manner. The non-dimensional number G_r can be written as

$$\begin{aligned} G_r &= \frac{g(\Delta_H/\tau)(H^2/\nu_V)H^3}{{\nu_V}^2}\left(\frac{H}{a}\right)^2 \\ &= \frac{gH\Delta_H}{a^2\Omega^2}\left(\frac{H^2\Omega}{\nu_V}\right)^3\frac{1}{\tau\Omega} \\ &= \frac{R_T}{E_V^3\tau\Omega} = R_T E_V^{-2}. \end{aligned} \tag{43}$$

Here, Eq. (41) is used in the third row. With Eqs. (41) and (42), A and B can be written as follows:

$$A = \pi^2\tau\Omega E_V = \pi^2, \tag{44}$$

$$B = 20\pi^2 E_H E_V = 2\pi^2 E_V^2 \times 10^4, \tag{45}$$

where $E_V/E_H = 10^{-3}$ is adopted as a constant according to M80. Here, A becomes constant because of Eq. (41), and B depends only on the vertical Ekman number. Let us denote $E_V^* \equiv 2\pi E_V$ for convenience. Using Eqs. (43)–(45), we can rewrite the equations for the boundaries (25), (27), (29), (32), and (34) described in Sections 3.3.a–3.3.e in E_V^* and $\sqrt{G_r}$, which are the horizontal and vertical axes in M80, respectively.

Figure 5a shows a regime diagram in E_V^*-$\sqrt{G_r}$ space. The corresponding original diagram is Fig. 10 in M80 and is shown in Fig. 5b. Note that the axes of the regime diagram by M80 are linear (Fig. 5b), whereas those in Fig. 5a are logarithmic to show a vast region in the parameter space. Dotted, dashed, double-dot-dashed, single-dot-dashed, and solid curves in Fig. 5a represent Eqs. (25), (27), (29), (32), and (34), respectively, in this parameter space. In the same manner as discussed in Sections 3.3.a–3.3.e, we can obtain approximated forms of

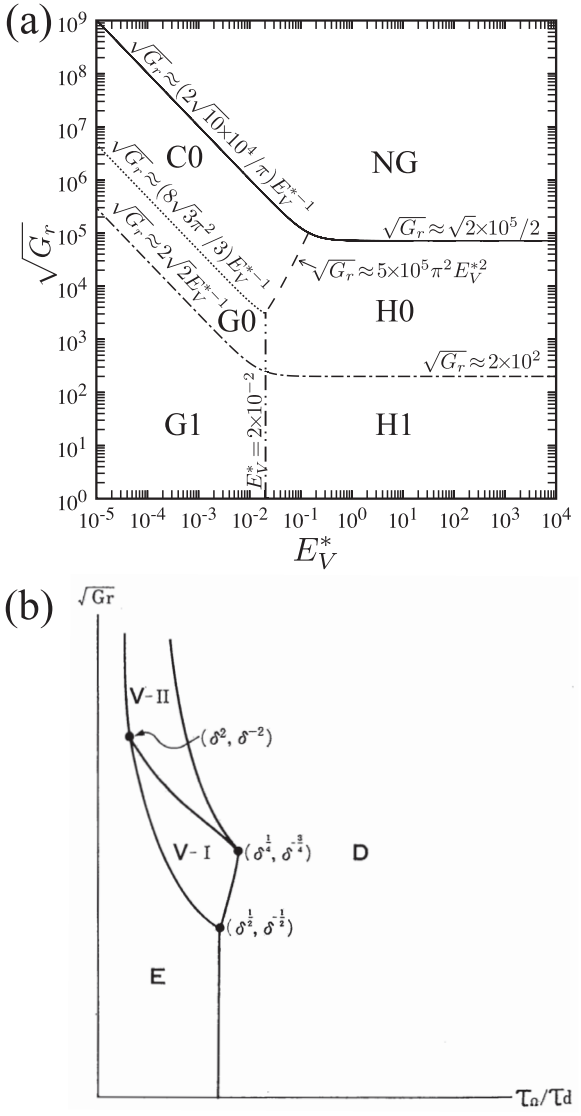

Fig. 5. (a) Same as upper panels of Fig. 1 but for a cross section in E_V^*-$\sqrt{G_r}$ parameter space with the constraints of $E_V^{-1} = \tau\Omega$ and $E_V/E_H = 10^{-3}$, where $E_V^* = 2\pi E_V = 2\pi/(\tau\Omega)$. (b) Matsuda's (1980) regime diagram for the similar situation as (a), from his Fig. 10. The symbols D and E denote the direct cell balance and the thermal wind balance of the Earth type, respectively, V-I indicates the region where only the solution in the thermal wind balance of the Venus type (V) exists, V-II indicates that where both the type D solution and the type V solution can exist as multiple equilibrium states, $\delta = E_V/E_H$, and $\tau_\Omega/\tau_d = E_V^*$ in this panel. Note that the axes in (a) are logarithmic, whereas those in (b) are linear.

the boundary equations for some limits of E_V^* or $\sqrt{G_r}$; they are also included in Fig. 5a.

Appearance of the $X0$ types, in which the equator-to-pole temperature difference is significantly reduced by the thermal advection, in Fig. 5a suggests the importance of the thermal advection by the mean meridional flow even in this cross section.

By ignoring whether the temperature difference is reduced ($X0$) or not ($X1$), we recognize that Fig. 5a almost corresponds to M80's regime diagram shown in Fig. 5b. That is, the parametric region of the cyclostrophic balance (CY and V) and that of the geostrophic balance (GY and E) occupy the similar locations in Figs. 5a and 5b. The region of horizontal diffusion balance (HY) in Fig. 5a corresponds to the lower half of the region of the direct cell balance (D) in Fig. 5b. The boundary between GY and HY expressed by $E_V^* = 2\times10^{-2}$ (double-dot-dashed line) also agrees with the corresponding boundary between the type E and the type D in Fig. 5b. The boundary between C0 and G0 (dotted line) has the dependence of $\sqrt{G_r} \propto E_V^{*-1}$ as shown in Fig. 5a; this qualitatively agrees with the boundary between V and E in Fig. 5b. On the other hand, the boundary between C0 and H0 (dashed line) approximately expressed as $\sqrt{G_r} \approx 5\times10^5\pi^2E_V^{*2}$ does not agree with the lower boundary between V and D.

The NG region, where Gierasch mechanism is expected not to function, may correspond to the upper half of the D region, where M80 predicted to be the direct cell balance. We should note that the differential rotation component considered in M80 could be dominant and the Gierasch mechanism would not be working in the D type solution in the upper half of the region in M80's third case (his Section 5). The NG type is located in the higher $\sqrt{G_r}$ region. In other words, the C0 region, where superrotation is expected to be maintained in cyclostrophic balance, in our model expands to a high $\sqrt{G_r}$ region, where the meridional difference of radiative thermal forcing is large, compared to the V region in M80. This might be due to the ignorance of the differential rotation component of the zonal wind in our theoretical framework in contrast to M80's model. We would like to note that YY13 showed numerically that the superrotation strength S can exceed the upper limit of S suggested in M80 (see Fig. 7 in YY13). Therefore, the upper limit of the C0 type solution in this parameter space could be higher than the corresponding limit in M80.

5.2 *Multiple equilibrium states*

It is notable that, in Fig. 3a, multiple equilibrium states are obtained in the region of NG, where the Gierasch mechanism is expected not to function. We have obtained two different solutions (shallow-jet and deep-jet) by time-integrations from different initial states (motionless and superrotation) for the same external conditions. The shallow-jet solution has a strong meridional circulation and the Gierasch mechanism does not function; in contrast, the deep-jet solution follows the theoretical model having a weak meridional circulation and the superrotation strength of about the theoretically estimated value (see YY13 for details of the solutions). Our numerical experiments showed that an equilibrium state achieved by time-integrations from the motionless initial state is significantly different between the CY and NG region in Fig. 3a. This result supports the validity of our consideration on the parametric limit given in Section 3.2. On the other hand, the presence of another equilibrium state that follows the theoretical model in the NG region leads the following discussion.

A key point for the multiple equilibrium states (or the initial-condition dependence in other words) may be the difference of the meridional wind speed at the top and just above the bottom: R_{vT} and R_{vB} in non-dimensional, respectively. We have expected that the Gierasch mechanism would not function when $R_{vB} > E_H$. Here, R_{vB} is used because it becomes much greater than R_{vT} when $S \gg 1$ according to Eqs. (8) and (9). Although our expectation is valid for generation of the superrotation from the motionless state, it is not necessarily valid for maintenance of the superrotation. We consider as follows: During the development of the superrotation from the motionless state, R_{vT} becomes greater than or comparable to E_H, and the meridional flow transports the angular momentum poleward against the horizontal diffusion (i.e., the Gierasch mechanism does not work). However, if the initial state is in a superrotation state and R_{vT} is much less than E_H, the superrotation can be maintained by the Gierasch mechanism.

As an example to show the different developments of meridional winds depending on the initial state, the time evolution of R_{vTn} (a measure of the meridional wind at the top) and R_{vBn} (just above the bottom) for $A = \pi^2 \times 10^{-1}$, $B = 2\pi^2 \times 10^{-2}$, $E_V = 10^{-3}$ is shown in Fig. 6.

Here, R_{vTn} and R_{vBn} are calculated from the numerical results by the following definitions

$$R_{vBn} \equiv -\frac{1}{a\Omega}\sum_{j=1}^{J} v(\phi_j, z_1)\cos\phi_j \Delta\phi_j, \tag{46}$$

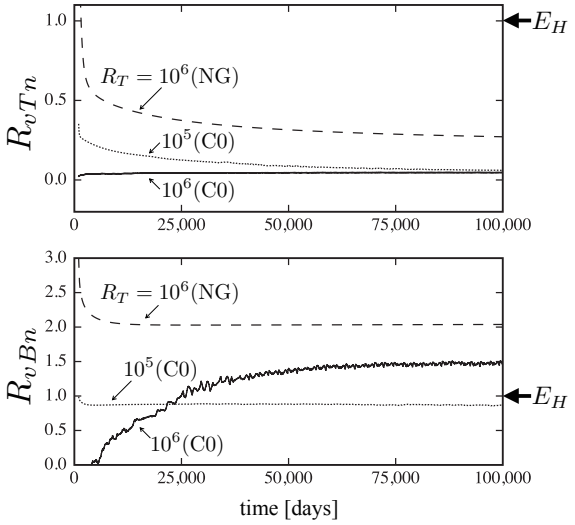

Fig. 6. Time evolution of R_{vTn} (top) and R_{vBn} (bottom) for $A = \pi^2 \times 10^{-1}$, $B = 2\pi^2 \times 10^{-2}$, and $E_V = 10^{-3}$. Dotted and dashed lines indicate the time evolution with $R_T = 10^5$ and 10^6, respectively, from the motionless initial state, and solid lines indicate that with $R_T = 10^6$ from a superrotation state. A 1000-day running mean is applied for smoothing. The value of E_H is shown in the right side.

$$R_{vTn} \equiv \frac{1}{a\Omega}\sum_{j=1}^{J} v(\phi_j, z_K)\cos\phi_j \Delta\phi_j, \tag{47}$$

respectively, where z_1 is the altitude of the lowest layer. Dotted and dashed lines indicate the time evolution with $R_T = 10^5$ and 10^6, respectively, from the motionless initial state, and solid lines indicate that with $R_T = 10^6$ from a superrotation state. When the time-integrations start from the motionless state, R_{vTn} is high in the initial stage. After the initial stage, in $R_T = 10^5$ case (dotted), R_{vTn} decreases to about 0.04, which is much less than $E_H = 1.0$; whereas, in $R_T = 10^6$ case (dashed), R_{vTn} decreases only to about 0.25, which is not much less than E_H. In $R_T = 10^6$ case with the superrotational initial state (solid), R_{vTn} is kept much less than E_H from the initial stage. On the other hand, R_{vBn} is comparable to E_H in both cases of $R_T = 10^6$ as shown in the lower panel of Fig. 6. These results suggest that the parametric limit considered in this study might be the boarder of the generation of the superrotation by the Gierasch mechanism but could not be that of the maintenance of the superrotation.

The abovementioned discussion suggests that the solution in the NG region might have at least two equilibrium states. However, there are some cases in which we did not obtain the multiple equilibrium states in the NG region. For example, we obtained C0 type solutions, which are in superrotation states, from the initial state of rest with $R_T = 10^5$ and 10^6 when $A = \pi^2 \times 10^0$ and $B = 2\pi^2 \times 10^{-3}$ as shown in Fig. 4b. This shows a possibility that the Gierasch mechanism works and generates a superrotational state from a non-superrotating state even with relatively small eddy diffusion of momentum (i.e., low $E_H \propto B$) in an atmosphere with a long radiative timescale (i.e., high $\tau \propto A$). This might be a favorable result for both Venus and Titan atmospheres because their radiative timescales in the lower parts are very long (Sánchez-Lavega 2010, Section 4.3.4). In Venus, the timescale near the surface should be important because the radiative and thermodynamic processes in the lower atmosphere could affect the strength of the meridional circulation, which is important in the Gierasch mechanism, even though the radiative timescale at the cloud top level, where the zonal wind reaches ~ 100 m s^{-1}, is relatively short.

5.3 *Very strong horizontal diffusion*

Very strong horizontal diffusion ($E_H \propto B$) with long radiative timescale ($\tau \propto A$) may prevent the Gierasch mechanism from maintaining the superrotation. For the cases of $R_T = 10^6$ and 10^7 with $A = \pi^2 \times 10^{-2}$ and $B = 2\pi^2 \times 10^0$, we have not obtained superrotation solution of C0 type (two cross signs in the C0 region in Fig. 4a) even though the theoretical regime diagram has predicted C0 type (not NG). The solid curve in Fig. 7 shows the meridional distribution of the relative angular momentum ($M_r \equiv ua\cos\phi$) at $z = H/2$ for $R_T = 10^7$ case of the abovementioned parameter values. The dashed curve shows $-a^2\Omega\cos^2\phi$: the relative angular momentum required for the absolute angular momentum [$M = (u + a\Omega\cos\phi)a\cos\phi$] to be vanished. Here, numerically obtained M_r is close to $-a^2\Omega\cos^2\phi$. That is, too strong horizontal diffusion leads M_r to be close to $-a^2\Omega\cos^2\phi$. We can understand that, because of such M_r-distribution, M becomes nearly zero and the angular momentum transport by the meridional circulation almost vanishes, and the superrotation cannot be maintained by the Gierasch mechanism.

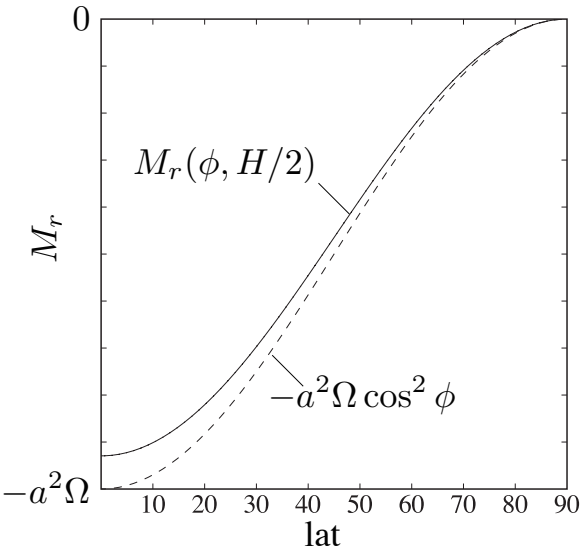

Fig. 7. Relative angular momentum M_r at $z = H/2$ of the steady state for $A = \pi^2 \times 10^{-2}$, $B = 2\pi^2 \times 10^0$, $R_T = 10^7$ (solid). Dashed curve shows $-a^2\Omega\cos^2\phi$.

6. Summary and conclusions

We have theoretically derived the regime diagrams that show the parametric dependence of the solution of a quasi-axisymmetric system of planetary atmospheres. The governing equations of the system are axisymmetric primitive equations for a dry Boussinesq fluid on a rotating hemisphere with strong horizontal diffusion terms parameterizing horizontal mixing by non-axisymmetric eddies. The fluid is forced by Newtonian heating and cooling. In this system, superrotation can be maintained by the Gierasch (1975) mechanism, which possibly explains the general circulation of the Venus atmosphere. In our previous study, Yamamoto and Yoden (2013, hereafter YY13), we developed a theoretical model of this system to estimate the superrotation strength defined by $S = U/(a\Omega)$ and found that the dominant dynamical balance can be classified into six types. (YY13 is briefly reviewed in Section 2.)

On the basis of these findings, in this study, we have defined the type of solutions of the governing equations (indicated by C1, C0, G1, G0, H1, and H0) and derived the Eqs. (25), (27), (29), and (32) describing the boundary of each type in a parameter space consisting of external non-dimensional numbers, R_T, $A = \pi^2\tau\Omega E_V$, and $B = 20\pi^2 E_H E_V$, from the theoretical model. Here, CY, GY, and HY mean a cyclostrophic balance, geostrophic balance, and horizontal diffusion balance, respectively, with $Y = 1$ for the equator-to-pole difference of the potential temperature close to the value for Newtonian heating and cooling or with

$Y = 0$ for a significantly smaller value of the difference; and R_T is the external thermal Rossby number, τ the radiative timescale, Ω the angular velocity of the planetary rotation, E_V the vertical Ekman number, and E_H the horizontal Ekman number. With E_V fixed, A can be regarded as a measure of the radiative timescale, and B can be regarded as a measure of the strength of horizontal diffusion.

We have obtained the upper limit of the superrotation strength as $S_L = E_H/(\pi^2 E_V) = B/(20\pi^4 E_V^2)$, which was not considered in YY13. This limit was derived by considering the parameter value with which the meridional overturning time becomes equal to the timescale of the horizontal diffusion in the model. Using S_L, we have also derived Eq. (34), which describes the parametric limit on the theoretical model in the regime diagrams.

Using the boundary equations described above, we have drawn four typical examples of the regime diagrams as shown in the upper panels of Figs. 1 and 2. These figures have clarified the dependence of the solution types on the measure of the radiative timescale A ($= \pi^2\tau\Omega E_V$) and that of the horizontal diffusion B ($= 20\pi^2 E_H E_V$) as well as the external thermal Rossby number R_T. The regime diagram of R_T-A cross section (Fig. 1) shows that the dynamical balance and the upper limit of the superrotation strength S_L, as well as the superrotation strength S itself, do not depend on the radiative timescale, if the radiative forcing is strong enough to keep the temperature almost radiative-convective equilibrium. On the other hand, if the radiative timescale is longer than the turnover time of the meridional circulation (its threshold is shown by Eq. (32) and single-dot-dashed curves in Fig. 1), S decreases as A increases and the dynamical balance also depends on A. From the regime diagram of R_T-B cross section (Fig. 2), we have found that the cyclostrophic balance CY, the most likely balance for Venus' atmosphere, is sandwiched between the horizontal diffusion balance HY and the parametric limit of the model (NG region) in B-direction. The width of the parameter range for CY solutions is mainly controlled by the vertical Ekman number E_V as shown in inequalities (37) and (38).

For a comparison with a regime diagram shown in M80, we have applied two constraints expressed as $E_V^{-1} = \tau\Omega$ and $E_V/E_H = 10^{-3}$ to our theoretical model, as adopted by M80. The axes of the regime diagram have been converted by Eqs. (43)–(45) to E_V^* and $\sqrt{G_r}$, the non-dimensional numbers used for axes in M80, where $E_V^* = 2\pi E_V$ and G_r is the Grashof number multiplied by the square of the aspect ratio. We have found that the regime diagram under above constraints in E_V^*-$\sqrt{G_r}$ space (Fig. 5a) is qualitatively same as that of M80 (Fig. 5b), except the appearance of the regions where the thermal advection is dominant denoted by X0, where X = C, G, or H. This is just because the effects of thermal advection by mean meridional flow were not considered in M80. However, the appearance of X0 region in the cross section same as M80 emphasizes the importance of thermal advection in the superrotation maintained by the Gierasch mechanism.

To verify the theoretical regime diagrams, we have performed time-integrations of the primitive equations to obtain numerical solutions in steady or statistically steady states for $R_T = 10^n$ (n = –2, –1, 0, ..., 7) with 14 combinations of the values of A and B, as listed in Table 1. The type of each solution has been numerically determined and compared with the theoretical regime diagrams, as shown in Figs. 3 and 4. In most region, the theoretical estimates of the solution type agree with the numerical results; whereas, some disagreement appears in high R_T regions. Superrotation solutions in the cyclostrophic balance with significant effects of thermal advection (C0 type) are obtained against the theoretical estimation that the Gierasch mechanism would not work (denoted by NG), when the radiative timescale is long (i.e., high A) and the horizontal diffusion is weak (i.e., low B) as shown in Fig. 4b. However, this disagreement shows a possibility that the Gierasch mechanism works with relatively small eddy diffusion of momentum in an atmosphere having a long radiative timescale such as that of Venus and Titan (Sánchez-Lavega 2010, Section 4.3.4).

We have obtained multiple equilibrium states in the predicted NG region shown in Fig. 3a. Time-integrations from a motionless state yielded a solution having a weak shallow equatorial jet with strong meridional circulation, in which the Gierasch mechanism seems not working; however, time-integrations from an initial state with strong zonal wind yielded a superrotational solution. This fact suggests that the parametric limit given by Eq. (34) or simply a lower limit of the horizontal Ekman number expressed in Eq. (36) would be a limit only for generating a superrotation state from a motionless state and not for just maintaining superrotational states.

This study has deepened our understanding of the

superrotation generated and/or maintained by the Gierasch mechanism, which possibly explains Venus' atmospheric general circulation. The obtained regime diagrams would be useful for future comparative studies on the superrotation of planetary atmospheres, even though the system we have explored is highly idealized and a comparison study using hierarchy of models with various levels of idealization is necessary as our future work.

Acknowledgments

We thank Professors Yoshihisa Matsuda, Takeshi Horinouchi, and two anonymous reviewers for helpful comments. The figures were produced by mjograph. This work was supported by JSPS KAKENHI Grant-in-Aid for JSPS Fellows 21·393.

References

Becker, E., 2001: Symmetric stress tensor formulation of horizontal momentum diffusion in global models of atmospheric circulation. *J. Atmos. Sci.*, **58**, 269–282.

Bengtsson, L., R.-M. Bonnet, D. Grinspoon, S. Koumoutsaris, S. Lebonnois, and D. Titov, 2013: *Towards Understanding the Climate of Venus*. Springer, 185 pp.

Bird, M. K., M. Allison, S. W. Asmar, D. H. Atkinson, I. M. Avruch, R. Dutta-Roy, Y. Dzierma, P. Edenhofer, W. M. Folkner, L. I. Gurvits, D. V. Johnston, D. Plettemeier, S. V. Pogrebenko, R. A. Preston, and G. L. Tyler, 2005: The vertical profile of winds on Titan. *Nature*, **438**, 800–802.

Counselman III, C. C., S. A. Gourevitch, R. W. King, G. B. Loriot, and E. S. Ginsberg, 1980: Zonal and meridional circulation of the lower atmosphere of Venus determined by radio interferometry. *J. Geophys. Res.*, **85**, 8026–8030.

Gierasch, P. J., 1975: Meridional circulation and the maintenance of the Venus atmospheric rotation. *J. Atmos. Sci.*, **32**, 1038–1044.

Gierasch, P. J., R. M. Goody, R. E. Young, D. Crisp, C. Edwards, R. Kahn, D. McCleese, D. Rider, A. Del Genio, R. Greeley, A. Hou, C. B. Leovy, and M. Newman, 1997: The general circulation of the Venus atmosphere: An assessment. *Venus II: Geology, Geophysics, Atmosphere, and Solar Wind Environment*. Bougher, S. W., D. M. Hunten, and R. J. Phillips (eds.), University of Arizona Press, 459–500.

Iga, S., and Y. Matsuda, 1999: A mechanism of the super-rotation in the Venus atmosphere: Meridional circulation and barotropic instability. *Theor. Appl. Mech. Japan*, **48**, 379–383.

Iga, S., and Y. Matsuda, 2005: Shear instability in a shallow water model with implications for the Venus atmosphere. *J. Atmos. Sci.*, **62**, 2514–2527.

Kido, A., and Y. Wakata, 2008: Multiple equilibrium states appearing in a Venus-like atmospheric general circulation model. *J. Meteor. Soc. Japan*, **86**, 969–979.

Kido, A., and Y. Wakata, 2009: Multiple equilibrium states appearing in a Venus-like atmospheric general circulation model with three-dimensional solar heating. *SOLA*, **5**, 85–88.

Luz, D., and F. Hourdin, 2003: Latitudinal transport by barotropic waves in Titan's stratosphere. I. General properties from a horizontal shallow-water model. *Icarus*, **166**, 328–342.

Matsuda, Y., 1980: Dynamics of the four-day circulation in the Venus atmosphere. *J. Meteor. Soc. Japan*, **58**, 443–470.

Read, P. L., 1986: Super-rotation and diffusion of axial angular momentum: II. A review of quasi-axisymmetrical models of planetary atmospheres. *Quart. J. Roy. Meteor. Soc.*, **112**, 253–272.

Rossow, W. B., and G. P. Williams, 1979: Large-scale motion in the Venus stratosphere. *J. Atmos. Sci.*, **36**, 377–389.

Sánchez-Lavega, A., 2010: *An Introduction to Planetary Atmospheres*. CRC Press, 629 pp.

Yamamoto, H., and S. Yoden, 2013: Theoretical estimation of the superrotation strength in an idealized quasi-axisymmetric model of planetary atmospheres. *J. Meteor. Soc. Japan*, **91**, 119–141.